Design of an interferometric system for the measurement of phasing errors in segmented mirrors

Carles Pizarro, Josep Arasa, Ferran Laguarta, Núria Tomàs, and Agustí Pintó

One of the new problems that has to be solved for segmented mirrors is related to periodic phasing, because for such mirrors to exhibit diffraction-limited performance the segments have to be positioned with an accuracy of a fraction of a wavelength. We describe the optical design of an instrument that measures the phasing errors (i.e., tip, tilt, and piston) between two segments under daylight conditions. Its design is based on a high-aperture white-light Michelson interferometer. It was developed at the Center for Sensors, Instruments and Systems Development (CD6) of the Technical University of Catalunya, Spain, and its final testing was carried out on the Gran Telescopio Canarias test workbench.

OCIS codes: 110.6770, 350.1260, 120.3180, 120.3930, 120.4570.

1. Introduction

In the early 1980s the astronomical community discussed the design of the next generation of telescopes, a generation that is now operative. The main issue that had to be resolved was the design and construction of a larger primary mirror. Scaling up the monolithic technology was not practical or affordable. Instead, the use of segmented mirrors, where many individual mirrors (the segments) work together to provide an image quality and an aperture equivalent to those of a large monolithic mirror, was considered a more appropriate strategy. However, for a segmented mirror to provide good optical performance, a phasing process is required in order to guarantee that each individual segment is properly positioned. For normal observing a positioning accuracy of tens of nanometers is needed,[1] but, when adaptive optics instruments are to be used, this accuracy has to be improved to a few nanometers.

The process of phasing a segmented mirror consists of determining the positioning errors between neighboring segments, which may be caused by relative rotations and displacements of the segments, and then removing the errors by using a set of actuators located under each segment. Once the initial misalignment has been removed, an active control system keeps the segments in their given initial positions. Figure 1(a) shows two contiguous segments and the reference system used hereafter, with the Z axis oriented in the intersegment direction. In this reference system the possible positioning errors of the segments are their relative rotations about the X axis (θ_X, or tilt) and the Z axis (θ_Z, or tip) and their relative vertical displacement along the Y axis [the piston error; see Fig. 1(c)].

The effects of the positioning errors mentioned above on the image of a distant star are substantially different, depending on whether these are rotational or vertical displacement errors. Relative rotations of the segments lead to relative displacements of the images of the distant source created by each individual segment. However, piston errors are displacements along the direction perpendicular to the segments [Fig. 1(c)]; they do not cause such displacements of the individual images but merely introduce a phase difference between the images of the source from each segment (leading to incoherent segment imaging).

In addition, piston measurements need to be made when relative rotations θ_X and θ_Z have been corrected to such an extent that they are not detectable by the piston measurement system. Otherwise, the piston error is not well defined, as it varies along the intersegment [Fig. 1(b)]. Obviously, because of the high-quality surface of the segments, noncontact optical measurement techniques are required for measure-

The authors are with the Center for Sensors, Instruments and Systems Development (CD6), Technical University of Catalunya, Rambla Sant Nebridi, 10 E-08222 Terrassa, Spain. C. Pizarro's e-mail address is pizarro@oo.upc.es.

Received 7 January 2002; revised manuscript received 18 March 2002.

0003-6935/02/224562-09$15.00/0

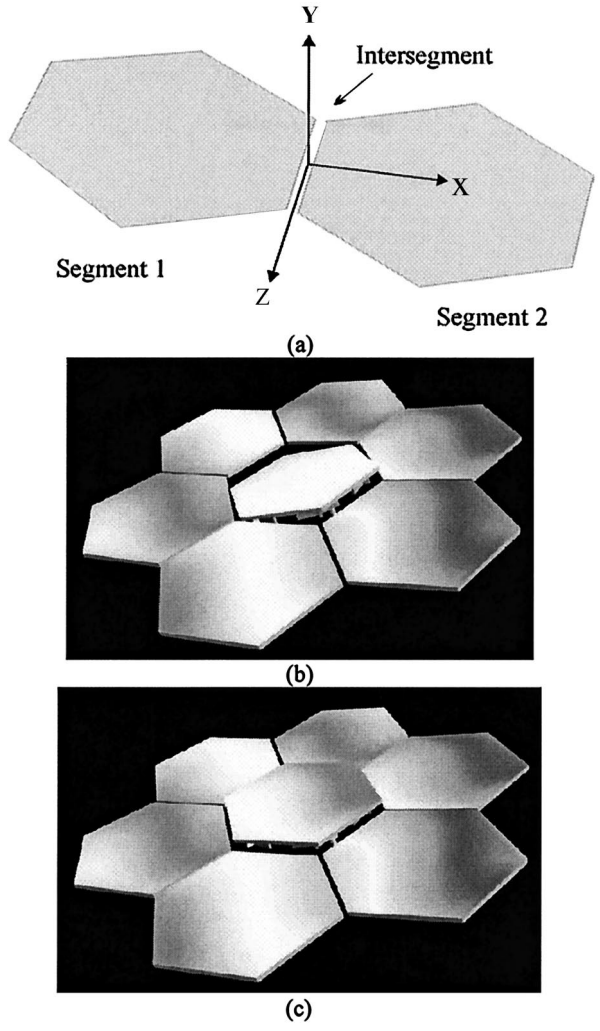

Fig. 1. (a) Reference system: the Y axis is defined along the direction locally perpendicular to the intersegment, and the Z axis is oriented along the direction of the intersegment. (b) Relative angular misalignment. (c) Relative vertical misalignment (piston). (b), (c) Images extracted from the GTC web site (http://www.gtc.iac.es).

ment of the initial misalignment. Whereas the control of tip–tilt for such mirrors has been demonstrated, absolute phasing (or piston control) presents a major challenge.[2] Various optical techniques have been proposed in the literature,[3,4] and they can be classified as follows: diffractive techniques,[1,5–8] curvature sensing techniques,[9–11] interferometric techniques,[12–15] and phase diversity techniques.[16–19] Diffractive techniques analyze the diffraction pattern produced by the intersegmental region in which the piston phasing error is to be determined. Curvature sensing techniques reconstruct the wave front from a pair of defocused images of a star imaged by the segmented mirror, one slightly inside and the other slightly outside focus. Interferometric techniques measure the piston error by analyzing the interference pattern produced either in a plane conjugated to the segmented mirror or locally at the intersegment zone. Phase diversity techniques use an iterative technique to find the pupil aberrations that best match the measured data obtained from a focused and a slightly defocused image.

Currently, only two segmented mirror telescopes are operative (the W. M. Keck telescopes), and some others are being built or designed [the Gran Telescopio Canarias (GTC) and the Telescopio Infrarojo Mexicano (TIM)]. The diffractive technique used in the Keck telescopes is based on a physical optics generalization of the Shack–Hartmann test. This technique has a repeatability of the order of 10 nm,[1,5] but it has the drawbacks that it uses starlight, as do most of the devices proposed for use as phasing systems, with the consequent loss of astronomical observational time, and that reducing piston errors from tens of micrometers to tens of nanometers requires an iterative technique (because of the small dynamic range of each iteration).

As was stated in *GTC Conceptual Design*[20]: "A technique should be implemented which allows the *phasing* of primary mirror segments without starlight so that it could be carried out *during daytime* without affecting the availability of observing time. This measurement can be carried out using an instrument which detects the discontinuities of the primary mirror in *local* intersegment zones." The instrument that is described in this paper was developed mainly to satisfy this requirement as well as others found in *GTC Conceptual Design*[20]: The technique should *not* require *interaction with the telescope* (e.g., stepping of the segments) and the *accuracy* in piston measurement should be *better than 5 nm* (needed when adaptive optics systems are used).

The paper is structured as follows: in Sections 2 and 3 the main decisions concerning the methodology and optical layout of the instrument are presented. Next, in Section 4, an optical analysis of the system is performed, showing that the proposed layout permits interferometric piston measurements to be made during daytime. In Section 5 there is some discussion of experimental results obtained in the laboratory that show the feasibility of the proposed instrument. Finally, in Section 6 our general conclusions are presented.

2. Methodology

As we said above, the work of designing a phasing system grew from the general requirements that can be found in *GTC Conceptual Design*.[20] We propose to use an interferometric technique to measure piston phasing errors, as these provide the nanometric accuracy that the measurement requires. Moreover, the main advantage of interferometric techniques is that they do not require using part of the telescope's observation time. Interferometers are able to operate during daytime—they may use their own internal light sources—yielding a daily increment in the effective observation time of the telescope compared with other phasing techniques.

The design of the phasing instrument, called UPC-

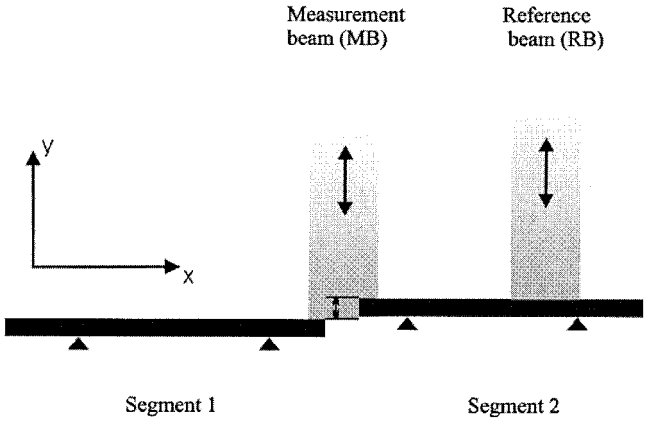

Fig. 2. The interferometric instrument: RB, reference beam; MB, measurement beam.

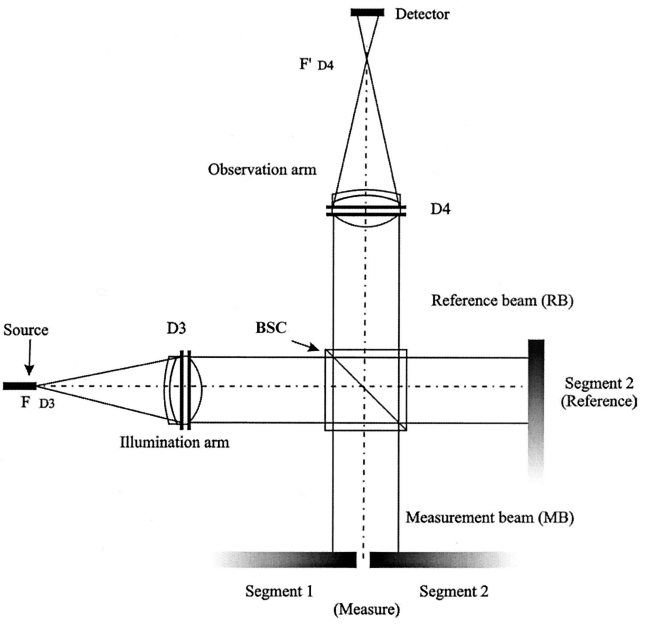

Fig. 3. Twyman–Green variation of the classic Michelson interferometer layout: F_{D3}, D3 focal object point; F'_{D4}, D4 focal image point; D3, D4, doublets; BSC, beam-splitter cube.

ZEBRA, is based on the well-known amplitude division Michelson interferometer. This kind of interferometer was chosen in preference to others such as the Mach–Zehnder[15] and the lateral-shift[12] interferometers because of its simple and versatile configuration and because it is able to fulfill the general requirements of a phasing instrument with few modifications.

To obtain the desired piston measurements we project the measurement beam of the interferometer (Fig. 2) onto the intersegmental region in a direction that is locally perpendicular to the segments, which was previously defined as the Y axis. This measurement beam is projected such that it evenly illuminates both segments. The reference beam of the interferometer is projected entirely onto one of the segments in a region situated as close as possible to the intersegment. It is also projected in the direction locally perpendicular to the segment at the projection point.

The presence of pistons between segments will lead to a phase step in the wave front reflected from the measurement region that will cause a fringe mismatch in the interference pattern, allowing the value of the piston to be measured. Each full fringe displacement is interpreted as a $\lambda/2$ piston phasing error. However, if only monochromatic light were used, piston phasing errors of multiples of $\lambda/2$ would yield identical fringe shifts, and absolute piston values could not be measured. To measure absolute values we also use white-light illumination in the instrument. Once the piston between a pair of segments has been measured, a robotic arm will position the interferometer on another intersegment and the measurement procedure will be repeated until all the intersegments have been measured.

3. Optical Layout

The starting point of the design is the Twyman–Green variation of the classic Michelson interferometer layout, depicted in Fig. 3. A beam-splitter cube (BSC) divides the light from a collimated source into the measurement and reference beams. Once the two beams are projected onto the intersegment region (measurement beam) and the region of one of the segments is used for reference (reference beam) the beams follow their paths backward and, after being recombined by the beam splitter, interfere on the CCD array placed at the end of the observation arm of the interferometer, which is in a plane that is conjugate to the segments. Using a region of one of the segments as a reference mirror has several advantages compared with the classic Twyman–Green optical test setup: It provides a high degree of both vibration insensitivity (as the same vibrations occur for both measurement and reference beams) and what is called wave-front matching, which means that, even though the primary mirror is a hyperboloid with typical values for the radius of curvature (R = 33 mm) and for the conicity ($k = -1.002250$), the interference pattern, given the geometry of the UPC-ZEBRA interferometer, will not vary significantly, regardless of the intersegmental region under analysis.

For mechanical reasons, however, the interferometer was built to work with its illumination and observation arms in a plane parallel to the segments. In this plane the illumination arm is rotated 45° with respect to the X axis and the observation arm is rotated 45° with respect to the Z axis, as depicted in Fig. 4. To guide the measurement and reference beams to the segments we place a pair of folding flat mirrors tilted at 45° (M2 and M3, Fig. 4) in both arms. As measuring the piston requires a number of fringes in the interferogram, mirror M3 is mounted upon a rotation stage, MP3, which allows the fringe period to be adjusted to the value required for the desired piston-error measurement range.

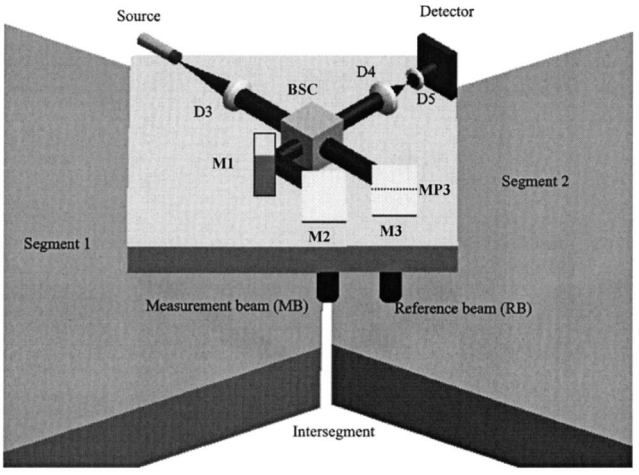

Fig. 4. Three-dimensional optical layout of the interferometer (the segments are not to scale). M1–M3, mirrors; D3–D5, doublets.

One consideration in the optical design of the interferometer is the simultaneous use of both monochromatic and white-light sources. Doing this will enforce a full geometrical symmetry between the measurement and reference arms of the interferometer, as no compensating plates can be used because of their high chromatic aberration.

An additional mirror, M1, is placed in the measurement beam path to desensitize the interferometer from small relative rotation positioning errors of the interferometer in the plane parallel to the segments (θ_X). In addition, to ensure full geometrical symmetry between the reference and measurement arms of the interferometer, a linear displacement stage is placed below mirror M1 such that the optical path difference between the reference and the measurement wave fronts can be set to zero during system alignment.

Another modification of the Twyman–Green layout is the introduction of an afocal imaging system in the observation arm. This system permits imaging of the segments in the CCD array while simultaneously reducing the size of the incoming wave front to match the CCD array size. Thus the simultaneous observation of the interference pattern and an image of the segments allows a direct phase assignment to be made to each point of the segments. Imaging the segments is also useful for aligning and positioning the interferometer. The observation arm was designed to be afocal to provide constant lateral magnification regardless of the working distance between the interferometer and the segmented mirror. Figure 5 shows schematically the final optical layout of the interferometer, including the afocal system just described. As we explained in Section 2, piston error values, measured when the relative angular misalignment between contiguous segments has been removed, will be extracted from the fringe mismatch in the interferogram.

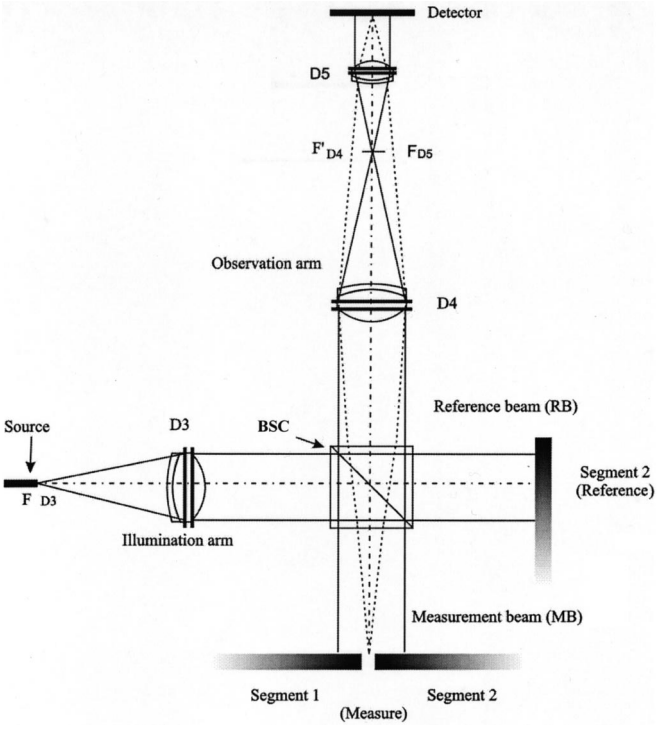

Fig. 5. Insertion of an afocal system into observation arms (D4 and D5) to image the intersegmental region on the detector plane combined with the interferogram fringes: F_{D3}, D3 focal object point, F'_{D4}, D4 focal image point; F_{D5}, D5 focal object point; D3 to D5, doublets; BSC, beam-splitter cube.

4. Design Analysis

Because the white-light interferograms will be used only to remove the $\lambda/2$ indeterminacy of a monochromatic interferogram, a detailed analysis of the white-light interferometric system is not required. However, as the nanometric accuracy of the measurement system relies on monochromatic interferograms, a detailed analysis of the optical performance under monochromatic illumination is carried out. The first issue to consider is the extension of the light source used, as it must ensure a sufficiently flat wave front before it strikes the beam-splitter cube. Next, an analysis of the quality of the measurement and reference wavefronts is made to ensure that the fringe mismatch in the interferogram is caused only by the piston between contiguous segments. This study is carried out under the assumption that the optical path difference between the reference and the measuring wave fronts has been completely compensated for and that relative rotations of the segments are so small as to be undetectable by the interferometer. Finally, the effect on the interfering wave front of the afocal imaging system is studied and analyzed to ensure that the interferogram remains unaltered.

The illumination arm contains a collimating system, which consists of an achromatic doublet (Fig. 5, D3) with f-number $N = 5.6$ and diameter 63.5 mm, with the light source placed in the object focal plane of the doublet. Such a large aperture is necessary for this component and for some others because a large observation area is needed to minimize the effect on measurement accuracy of segment polishing

errors, which are expected to be higher close to the segment edges. The light source for the interferometer is an optical fiber coming from an external illumination system. The system contains a halogen lamp and a set of filters to select white light or monochromatic illumination. We obtain the monochromatic source by inserting a bandpass interferential filter centered at 632.8 nm with a FWHM of 10 nm. To obtain the same illumination level on the CCD array when white light is used, we insert a 2 OD (optical-density) neutral-density filter. The light source will have the size of the core of the optical fiber used, which has a diameter of 600 μm. The first thing that has to be done is to evaluate the effect of this extension on the collimation quality of the wave front leaving collimator D3. The optical path maps of the collimated wave front leaving D3 on-axis [Fig. 6(a)] and at the edge of the source [$d = 300$ μm; Fig. 6(b)] are presented as contour plots with a contour step height of λ/100; the central wavelength of the interference filter (632.8 nm) is used. We calculated the values at the edge of the source by subtracting the path difference caused by the wave-front tilt associated with a light source placed off-axis (the paraxial component hereafter). This component does not play an important role in the interferogram, as each point in the incident wave front is interfering with itself, and the phase differences in the two arms are those that lead to the final intensity value.

The results in Fig. 6 show how, for a source placed on-axis, the wave-front departure from a perfectly collimated wave front remains less than 5λ/100. The maximum divergence value in the collimated beam is less than 1.7×10^{-3} rad. The results for a point source placed at the edge of the field are equivalent, once the paraxial component has been subtracted. This deviation from the perfect beam is well within the collimation requirements for a wave front striking the beam-splitter cube to produce interferograms that allow nanometric distance measurements. This means that the wave front at the output of the imaging system is no longer required to be flat; any wave front is valid as long as the imaging system does not overlap different wave fronts coming from different points of the light source. If it did, a loss of contrast would be observed. The equivalence of behavior of an on-axis and a field point source guarantees good interferogram quality (contrast). The wave-front asymmetry that can be seen in Fig. 6 is due to small positioning errors of optical elements, because for this instrument the mechanical positioning precision is 1 μm. This asymmetry is also present in other wave fronts (Figs. 7–9), but it is observable only in Figs. 6 and 9. As we shall see, this asymmetry will have no effect on measurement accuracy.

Next, the effect of the beam-splitter cube on wave-front quality is analyzed. To isolate the optical effects of the beam-splitter cube we have assumed reflection onto perfect segments precisely aligned in the absence of relative rotation and piston errors. It has also been assumed that the beam splitter is perfect and has a transmission/reflection ratio of 50:50. The beam splitter's effect on wave-front quality will again be different for an on-axis source and for a field source. Figure 7 shows a plot equivalent to that of Fig. 6 but after the wave fronts have crossed the beam-splitter cube twice. The contour step curves of the optical path differences are again plotted with a contour step height of λ/100. Again, the on-axis source yields departures from the perfectly flat wave front of less than λ/20 [Fig. 7(a)], whereas the field source [Fig. 7(b)] yields an equivalent wave front with departures from the perfectly collimated beam also remaining less than λ/20 once the paraxial component of the wave front is removed. It should be noted that the wave front is not degraded after it crosses the beam splitter twice, as the degree of de-

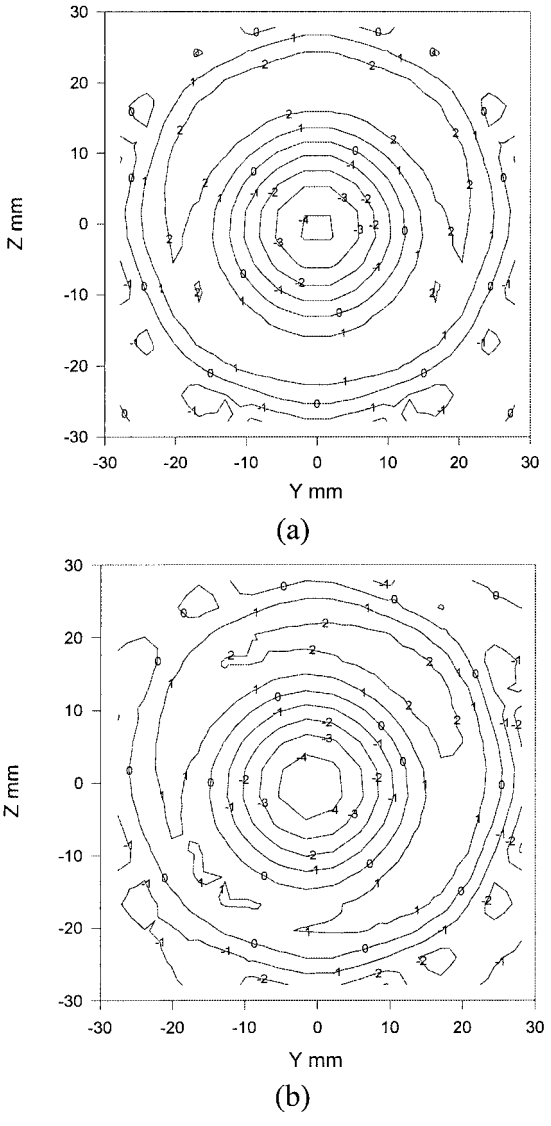

Fig. 6. Optical path maps after the wave front leaves the D3 collimator, presented as contour plots: (a) point light source on axis, (b) point light source placed at the edge of the object field of the collimator (300 μm) when the paraxial component has been subtracted (λ = 632.8 nm; contour step λ/100).

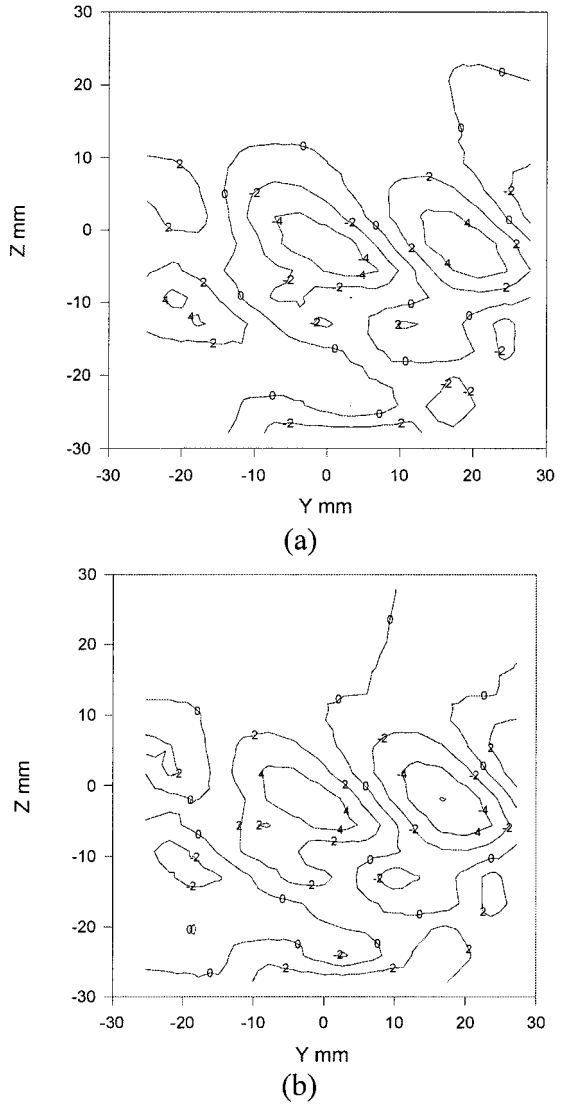

Fig. 7. Optical path maps after the wave front leaves the beam-splitter cube, presented as contour plots: (a) point light source on axis; (b) point light source placed at the edge of the finite extent of the source (300 μm) when the paraxial component is subtracted (λ = 632.8 nm; contour step λ/100).

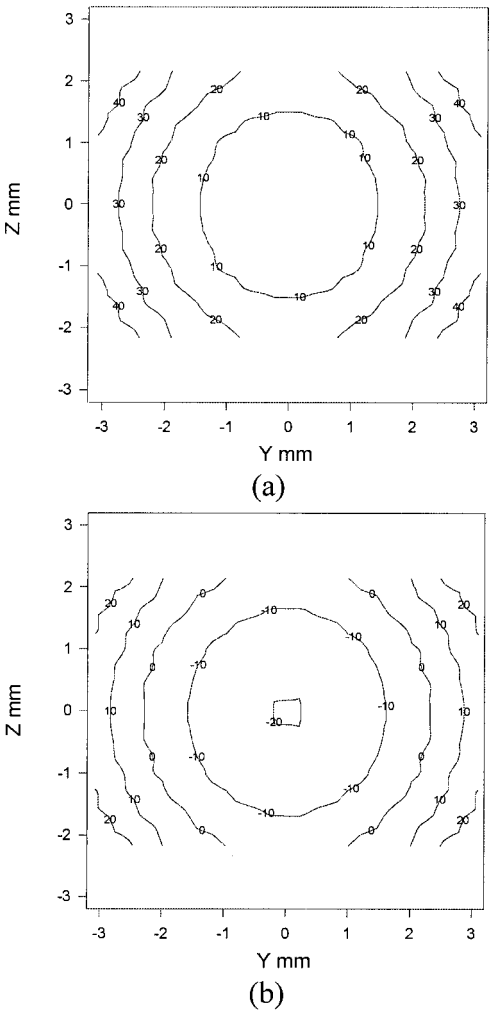

Fig. 8. Optical path maps after the wave front crosses crossing the afocal imaging system, presented as contour plots: (a) point light source on axis, (b) point light source placed at the edge of the finite extent of the source (300 μm) when the paraxial component has been subtracted (λ = 632.8 nm; contour step λ/10). Note the equivalence of the two plots, which ensures that the afocal system does not distort the interferograms that are recorded.

parture from the flat wave front is the same as it was before the wave front crossed the cube.

The last step in our analysis considers the effect on the interferograms of the afocal system introduced in the observation arm to image the intersegmental region at the same time as the interference pattern. The equivalence of the wave fronts obtained from a point source placed on-axis and at the edge of the source should still be observed in the wave fronts that are leaving the afocal system. These wave fronts will no longer be flat, but, to permit adequate interferogram fringe observation, the afocal imaging system should not introduce phase differences between the on-axis and the edge-of-field wave fronts.

The detector is a 768 by 576 pixel CCD array placed in a plane conjugated to the segments of the afocal system with a lateral magnification of $m = 0.14$ determined by the required object and image sizes. The system works with a maximum field of view of 1.7×10^{-3} rad owing to the finite extension of the light source and permits the simultaneous imaging of the intersegment region with a field of view of 45.3 mm by 34 mm, enough for our piston measurement purposes, and the interference pattern.

Following the optical path difference plots in Figs. 6 and 7, Fig. 8 depicts the optical path differences from an axial light source [Fig. 8(a)] and a point source placed at the edge of the field [Fig. 8(b)] with the paraxial component removed, after the light passes through the afocal imaging system placed in the observation arm. To achieve a good-quality imaging system combined with interferogram fringe observation, we allow the afocal system to change the convergence of the incoming wave front (a 4λ optical path difference variation may be observed in the

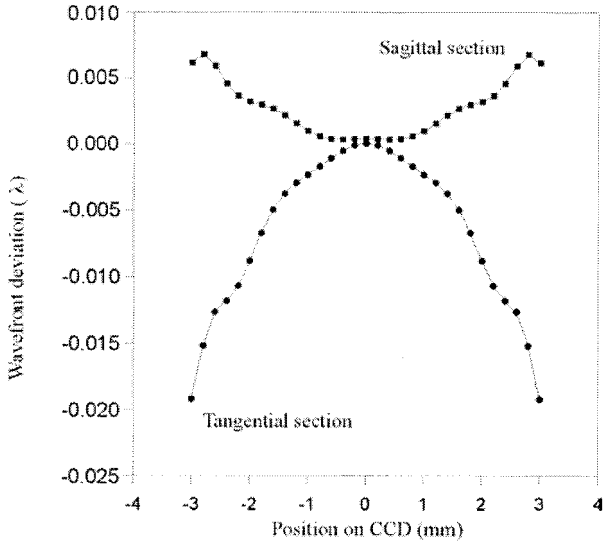

Fig. 9. Deviations along the tangential and sagittal sections of the wave fronts depicted in Fig. 8, corresponding to an on-axis and an edge-of-field point light source. The maximum deviation remains less than $\lambda/50$.

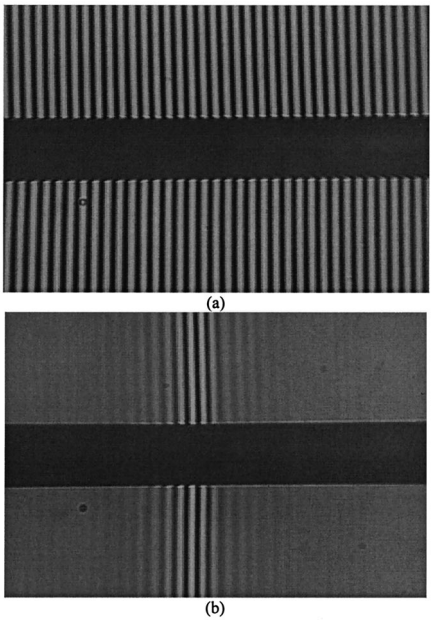

Fig. 10. Real interferograms obtained with the instrument that we have designed in a piston-phasing-error measurement range of 12 μm. The actual piston is 0 μm (phased segments): interferograms obtained with (a) monochromatic light (λ = 632.8 nm) and (b) white light.

wave front), although the system does not introduce phase changes in addition to those that are present in the incident wave front. This means that the wave front leaving the optical system is no longer flat, although it keeps a constant shape for all possible source field values. These features may be appreciated from Fig. 8 for sources on the axis and at the edge-of-field values. To verify that this behavior is correct we calculated the differences in the wave fronts plotted in Fig. 8 at a set of points along their tangential and sagittal sections; the deviations have been plotted in Fig. 9. Wave-front deviations obtained from the edge-of-field point source relative to the on-axis source may be seen always to be less than the $\lambda/50$ value, which ensures that the interferogram fringes will not be noticeably affected by the aberrations introduced by the afocal system. As in Fig. 6, the asymmetry that can be observed in this figure is due to small positioning errors of optical elements, because for this instrument the mechanical positioning precision is 1 μm. This analysis allows us to state that interference fringe mismatching will be caused only by errors in the relative positioning of the pair of contiguous segments under analysis. From Figs. 6–8 the optical quality of the optics to be used can also be extracted: $\lambda/20$ optical quality is needed.

5. Results

We used the layout described above to build an interferometric piston-phasing-error measurement instrument. The interferometer was designed and built at the Center for Sensors, Instrumentation and Systems Development of the Technical University of Catalunya and tested at the Gran Telescopio Canarias test workbench.

As expected, the imaging system permits a clear vision of the area being tested, which is made from three clearly separated regions [Figure 10(a)], namely, the upper subfield, where the reference wave front (from segment 2) interferes with the half of the measuring wave front that comes from segment 1; the intersegment area; and the lower subfield, where the reference wave front interferes with the half of the measuring wave front that comes from the same segment (segment 2). The presence of a piston will lead to fringe mismatching in the interference pattern, which will become evident when white-light illumination is used [see Fig. 11(b)]. Residual tip and tilt angular misalignment will also have an effect on the upper subfield fringe pattern, allowing it to be extracted as well: Relative tilt between segments will cause the fringe period to change, and relative tip will cause the fringes to deviate from the vertical.

Figures 10 and 11 show representative interferograms registered on the CCD array and used for piston-error determination. The piston measurement range was set to 12 μm, but the actual piston in each figure is different: in Fig. 10 the piston is zero and in Fig. 11 the piston is close to 8 μm. Figures 10(a) and 11(a) show a monochromatic interferogram; whereas Figs. 10(b) and 11(b) are white-light interferograms. Note how the $\lambda/2$ indeterminacy that is intrinsic in monochromatic interferograms is easily removed by use of white-light illumination. It is also interesting to note that the number of observed fringes in the interferograms can be adjusted by use of rotation axis MP3 on mirror M3 to obtain the desired value for the piston measurement range, which is limited only by the fringe sampling at the CCD array. Laboratory tests have shown that the system

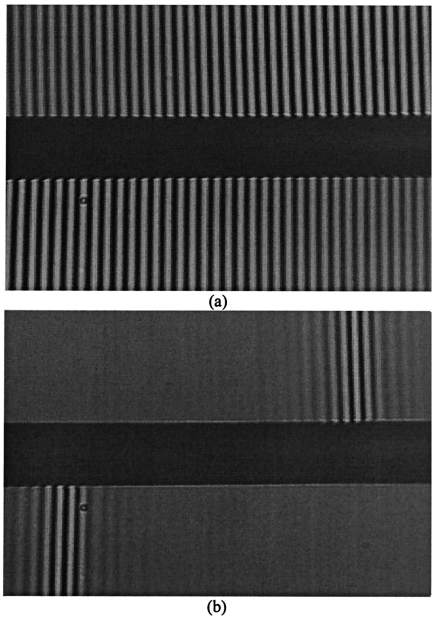

Fig. 11. Real interferograms obtained with the instrument that we have designed in a piston-phasing-error measurement range of 12 μm. The actual piston is +8 μm. Interferograms obtained with (a) monochromatic light (λ = 632.8 nm) and (b) white light.

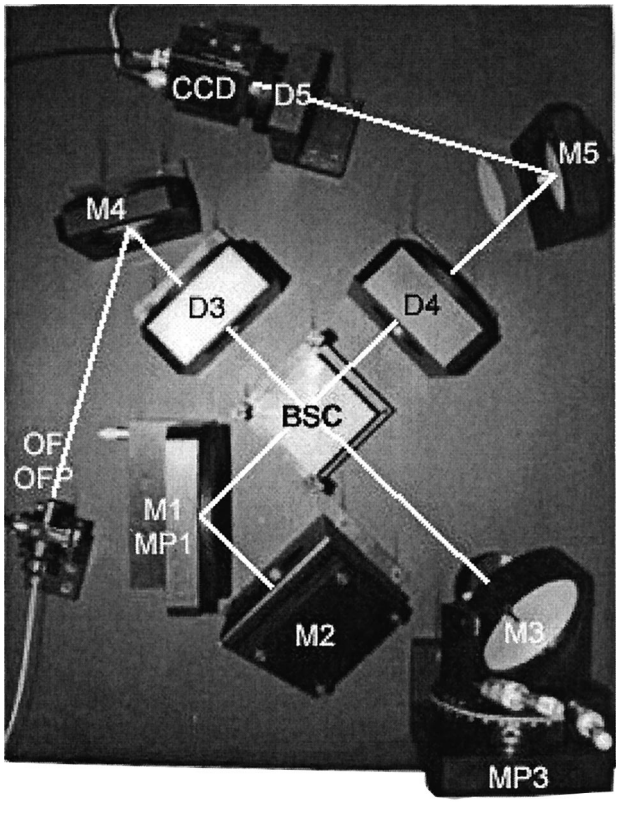

Fig. 12. Picture of the phasing instrument in the laboratory: OF, optical filter; OFP, optical filter positioner; M1–M5, mirrors; MP1, MP3, mirror positions; BSC, beam-splitter cube; D3–D5, doublets.

is able to measure a piston range of 12 μm between segments with a repeatability of 5 nm rms as well as residual tip and tilt misalignments. A picture of the phasing instrument is shown in Fig. 12. Additional folding mirrors, M4 and M5, were placed in the illumination and observation arms, respectively, to reduce the dimensions of the instrument. Also, M1 was provided a displacement positioner (MP1) for optical path difference balancing. The system's performance has also been tested on the GTC test bench under workshop conditions.

6. Conclusion

The interferometric piston-phasing-error measurement system presented here has the desirable property of being able to carry out the phasing of a segmented mirror during daytime, saving valuable observation time for scientific purposes. Moreover, the dynamic range has been increased with respect to those of other phasing techniques that have been proposed, e.g., the one used at the Keck telescopes. We propose mounting the interferometer upon a robotic arm and measuring the piston phasing error locally at each intersegment. This procedure has the advantages that the primary segmented mirror of a telescope can be phased during daytime while the telescope is pointing at the expected observation region of the sky and thus will suffer no gravitational stresses and also that the segmented mirror can be phased again less than 10 min a segment after being exchanged.

An optical design of an interferometer for the local measurement of piston-phasing errors in segmented mirrors has been described. Starting with a classic Michelson interferometer layout, a set of modifications was introduced to make it suitable for use as a phasing instrument. Folding mirrors are used to guide the beams along the required direction such that the reference beam of the interferometer falls on one of the segments, and the measurement beam is equally divided between the two contiguous segments whose misalignment is to be measured. An afocal imaging system placed in the observation arm permits imaging of the intersegmental region without distorting the interferograms. Piston-error measurements will be obtained from the fringe mismatch in the interferogram. Both monochromatic and white-light interferograms will be obtained to solve the λ/2 indeterminacy. A detailed analysis of the wave-front quality as it travels along the various optical elements of the interferometer has been performed, showing the validity of the proposed interferometer design. Finally, some results obtained at the test workbench and in the lab have been shown, which provide consistent proof of the capability of the proposed instrument to determine accurately the piston phasing error in segmented mirrors during daytime, with the required nanometric repeatability. Lab tests have also shown that the system is able to measure residual tip and tilt misalignments.

This study was financed by the Comisión Interministerial de cienca y Tecnología (Spain) through the Programa Nacional de Tecnologías Avanzadas de la Producción (TAP96-1043), and by GRANTECAN S.A. A. Pintó thanks the Departament d'Universitats, Recerca i Societat de la Informació (Catalunya regional government), for the PhD grant he received, which permitted him to take part in this research.

References

1. G. Chanan, M. Troy, F. Dekens, S. Michaels, J. Nelson, T. Mast, and D. Kirkman, "Phasing the mirror segments of the Keck telescopes: the broadband phasing algorithm," Appl. Opt. **37,** 140–155 (1998).
2. G. Chanan, J. Nelson T. Mast, P. L. Wizinowich, and B. Schaefer, "W. M. Keck Telescope phasing camera system," in *Instrumentation in Astronomy VIII*, D. L. Crawford and E. R. Craine, eds., Proc. SPIE **2198,** 1139–1150 (1994).
3. M. Owner-Petersen and T. Andersen, "Overview of optical metrology for segment phasing," in *Workshop on Extremely Large Telescopes* (E. Jurlander, Lund, Sweden, 1999), pp. 152–161.
4. A. Schumaker, L. Montoya, N. Devaney, K. Dohlen, and P. Dierickx, "Phasing ELT's for adaptive optics: preliminary results of a comparison of techniques," presented at the *Beyond Conventional Adaptive Optics Conference*, Venice, Italy, 7–10 May 2001.
5. G. Chanan, C. Ohara, and M. Troy, "Phasing the mirror segments of the Keck telescopes II: the narrow-band phasing algorithm," Appl. Opt. **39,** 4706–4714 (2000).
6. A. Weitheimer and T. Dey, "Wide-range, high-accuracy, white light piston sensor for segmented optics," Opt. Eng. **34,** 2149–2156 (1995).
7. J. T. Watson, "Experimental study of mirror segment phasing using tungsten light," Opt. Eng. **27,** 758–761 (1988).
8. N. C. Mehta and C. Allen, "Remote alignment of segmented mirrors with far-field optimization," Appl. Opt. **31,** 6510–6518 (1992).
9. G. Chanan, M. Troy, and S. Sirko, "Phasing the Keck telescopes with out-of-focus images in the infrared," Appl. Opt. **38,** 704–713 (1999).
10. V. G. Orlov, S. Cuevas, F. Garfias, V. V. Voitsekhovich, and L. J. Sanchez, "Co-phasing of segmented mirror telescopes with curvature sensing," in *Telescope Structures, Enclosures, Controls, Assembly/Integration/Validation, and Commissioning*, T. A. Sebring and T. Andersen, eds., Proc. SPIE **4004,** 540–551 (2000).
11. J. M. Rodriguez-Ramos and J. J. Fuensalida, "Phasing segmented mirrors: new algorithm and numerical results for piston detection," in *Optical Design, Materials, Fabrication and Maintenance*, P. Dierickx, ed., Proc. SPIE **4003,** 270–278 (2000).
12. H. W. Klumpe, B. A. Lajza-Rooks, and J. D. Blum, "Absolute phasing of segmented mirrors using the polarization phase sensor," Rev. Sci. Instrum. **63,** 1698–1706 (1992).
13. R. F. Horton, E. E. Huber, L. A. Bernotas, L. G. B. Yee, A. V. Roberts, J. M. Norton, E. G. Corbett, and R. A. Humphreys, "Absolute piston phasing of segmented-mirror optical systems using depth-modulated white-light interferometry," in *Advanced Technology Optical Telescopes IV*, L. D. Barr, ed., Proc. SPIE **1236,** 974–984 (1990).
14. K. Dohlen, F. Decortiat, F. Fresneau, and P. Lanzoni, "Dual-wavelength random-phase-shift interferometer for phasing large segmented primaries," in *Advanced Technology Optical/IR Telescopes VI*, L. M. Stepp, ed., Proc. SPIE **3352,** 551–559 (1998).
15. B. Jacobsen and R. Angel, "High accuracy wavefront stellar wavefront sensing using a Zernike interferometer," Bull. Am. Astron. Soc. **26,** 1373–1381 (1994).
16. R. G. Paxman and J. R. Fienup, "Optical misalignment sensing and image reconstruction using phase diversity," J. Opt. Soc. Am. A **5,** 914–922 (1988).
17. R. L. Kendrick, D. S. Acton, and A. L. Duncan, "Phase diversity wavefront sensor for imaging systems," Appl. Opt. **33,** 6533–6546 (1994).
18. M. G. Lofdahl, R. L. Kendrick, A. Harwit, K. E. Mitvhell, A. L. Duncan, J. H. Seldin, R. G. Paxman, and D. S. Acton, "A phase diversity experiment to measure piston misalignment on the segmented primary mirror of the Keck II telescope," in *Space Telescopes and Instruments V*, P. Y. Bely and J. B. Breckinridge, eds., Proc. SPIE **3356,** 1190–1201 (1998).
19. S. A. Basinger, D. C. Redding, A. E. Lowman, L. A. Burns, K. Y. Liu, and D. Cohen, "Performance of wavefront sensing and control algorithms on a segmented telescope testbed," in *UV, Optical and IR Space Telescopes and Instruments*, J. B. Breckinridge and P. Jakobsen, eds., Proc. SPIE **4013,** 749–756 (2000).
20. GTC Project Office, ed., GTC Conceptual Design (Grantecan S.A. 1997), http://www.jtc.iac.es.